

Your Interlibrary Loan request has been sent by email in a PDF format.

If this PDF arrives with an incorrect OCLC status, please contact lending located below.

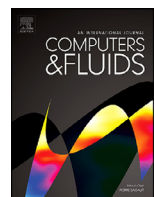
Concerning Copyright Restrictions

The copyright law of the United States (Title 17, United States Code) governs the making of photocopies or other reproductions of copyrighted materials. Under certain conditions specified in the law, libraries and archives are authorized to furnish a photocopy or other reproduction. One of these specified conditions is that the photocopy or reproduction is not to be "used for any purpose other than private study, scholarship, or research". If a user makes a request for, or later uses, a photocopy or reproduction for purpose in excess of "fair use", that user may be liable for copyright infringement. This institution reserves the right to refuse to accept a copying order if, in its judgment, fulfillment of the order would involve violation of copyright law.

Interlibrary Loan Services: We Search the World for You...and Deliver!

Interlibrary Loan Services – FSU Community
James Elliott – Resource Sharing Manager
The Florida State University
R.M. Strozier Library
116 Honors Way
Tallahassee, Florida 32306-2047
Email: lib-borrowing@fsu.edu
Website: <https://www.lib.fsu.edu/service/interlibrary-loan>
Phone: 850.644.4466

Non-FSU Institutions:
Lib-Lending@fsu.edu
850.644.4171



Benchmark solutions

Detailed numerical simulations of pore competition in idealized micro-spall using the VOF method

L.C. Malan ^{a,b,c,*}, Y. Ling ^{a,b,d}, R. Scardovelli ^e, A. Llor ^f, S. Zaleski ^{a,b}^a Sorbonne Universités, UPMC Univ Paris 06, UMR 7190, Institut Jean le Rond d'Alembert, F-75005, Paris, France^b CNRS, UMR 7190, Institut Jean le Rond d'Alembert, F-75005, Paris, France^c InCFD, Dept. Mechanical Engineering, University of Cape Town, Cape Town 7701, South Africa^d Department of Mechanical Engineering, Baylor University, Waco, Texas 76798, United States of America^e DIN-Laboratorio di Montecuccolino, Università di Bologna, 40136 Bologna, Italy^f CEA, DAM, DIF, 91297 Arpajon Cedex, France

ARTICLE INFO

Article history:

Received 3 May 2017

Revised 8 May 2019

Accepted 14 May 2019

Available online 15 May 2019

Keywords:

Micro-spall

Pore competition

Volume-of-Fluid

Bubbles

Cavitation

Free-surface

ABSTRACT

Under shock loading, metals have been found to melt and with reflection of the shock wave from the material free surface, cavities nucleate and grow. This process is referred to as *microspalling* and has been the topic of several experimental investigations. Measurements during the cavity growth phase are not possible at present and we present here a Detailed Numerical Simulation of an idealized problem where we assume an inviscid, incompressible liquid subject to a constant expansion rate with cavities at a vanishing vapour pressure.

To allow for a time-varying gas volume a free-surface interface condition has been implemented in an existing incompressible multiphase Navier-Stokes solver, PARIS, using a Volume-Of-Fluid method. The gas flow remains unsolved and is instead assumed to have a fixed pressure which is applied to the liquid through a Dirichlet boundary condition on the liquid-gas interface. Gas bubbles are tracked individually, allowing the gas pressure to be prescribed using a suitable equation of state.

Simulations with hundreds of bubbles have been performed in a fixed domain under a constant rate of expansion. A bubble competition is observed: larger bubbles tend to expand more rapidly at the demise of smaller ones. The time scale of this competition is shown to depend on the Weber number.

© 2019 Elsevier Ltd. All rights reserved.

1. Introduction

Andriot [1] is cited by Signor [2,3] as the first to have used the term *microspalling*. Micro-spall refers to the fine spray of ejecta formed from melted material after failure of a material under shock loading [3]. The process is described by Signor [3]: dynamic stress loading on material samples creates a compression wave that propagates through it. Upon reflection from the free surface of the sample, tensile stresses are created in the material that cause the nucleation of cavities. These cavities may grow up to coalescence and lead to fine droplets of melted material being formed as the material fails [2]. A schematic representation of this process is taken from Signor et al. [4] and shown in Fig. 1.

Microspalling has been studied experimentally [4–6]. Some analytical models have been created to predict the debris sizes measured in these experiments, which provide global perspectives on

void fraction evolution and debris sizes [3,7–9]. Theoretical investigations into micro-spalling have also been made. Stebnovskii, for example, conducted several investigations, including the formation conditions for vapour bubbles during cavitation [10], a shear deformation model [11] and a rheological model of the media during cavitation [9]. In [3], Signor proposes a hollow sphere model to investigate the dynamics of cavities using analytical models. Several liquid dilatation rates for typical shock loading times are applied to the hollow sphere model and the evolution of the total porosity is studied. The main question posed by that author is whether the kinetic energy transferred to the liquid from the loading is sufficient to lead to percolation.

It is this competition between the expansion of the volume and the energy required to sustain it that forms the focus of our investigation. Present experimental methods cannot study the detail physics in the melted material, due to the complex nature of the process and the time and length scales involved. We therefore propose to create a simplified model problem of the cavitation process prior to the ejection of micro-spall and then to study it using a Detailed Numerical Simulation. By this term, we mean that we solve

* Corresponding author at: InCFD, Dept. Mechanical Engineering, University of Cape Town, Cape Town, 7701, South Africa.

E-mail address: leon.malan@uct.ac.za (L.C. Malan).

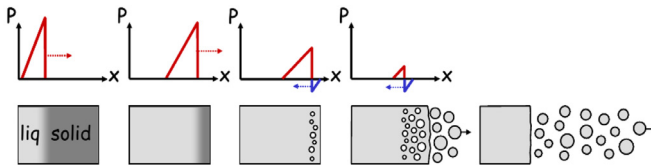


Fig. 1. A schematic representation of the micro-spall process by Signor [4]. A compression wave is shown by the pressure plot at the top and moves from left to right through the material sample. As the wave reaches the free surface on the right, it is reflected and vapour bubbles are nucleated from the resulting tension in the material. If bubbles grow sufficiently large to percolation, droplets are formed that get ejected by the residual momentum in the material post shock.

in three dimensions a set of governing equations up to a resolution where the dominant physics for the simplified model problem of microspalling is captured.

The model problem consists of an incompressible, inviscid liquid containing several gas bubbles. The inviscid assumption is based on the very small Ohnesorge number (Oh) encountered in micro-spall fracture experiments with tin samples. Typical tin samples have a thickness of the order of $100 \mu\text{m}$. If we consider the length scale of the small debris in laser irradiation and plate impact experiments, $L \approx 10 \mu\text{m}$ [4], we have

$$Oh = \frac{\mu}{\sqrt{\rho\sigma L}} = 5.5 \times 10^{-3} \quad (1)$$

with $\mu = 10^{-3} \text{ Pa.s}$, $\rho = 6.5 \times 10^3 \text{ kg.m}^{-3}$ and $\sigma = 0.5 \text{ N.m}^{-1}$ the dynamic viscosity, density and surface tension of liquid tin. Our model will include the effects of surface tension at the vapour-liquid boundary, as this will be a crucial effect governing the size distribution of vapour bubbles in the expanding liquid. Thermal effects are not considered in this idealized problem and the carrier fluid density and surface tension coefficient are treated as constants. The effect of gravity is considered negligible. The cavity nucleation process will not be modelled, but small spherical vapour bubbles will be assumed to already exist in the carrier liquid.

The next section will discuss existing methods to deal with this model problem or similar problems, after which our approach will be stated.

1.1. Existing numerical work

Bubble clouds during cavitation or its interactions with shocks have been the topic of investigation in several theoretical studies employing mathematical models. A prominent example is the study of pressure wave propagation in liquids filled with bubbles in the dilute limit by Watanabe and Prosperetti [12]. Another example is the study by Fuster et al. [7], where the potential energy in the system is considered as a critical factor in the interaction between bubble clouds and their carrier liquid under tension.

Studies on single bubbles have been performed using different interface tracking techniques with a one-fluid formulation of the governing equations. Popinet used marker particles to study the collapse of vapour bubbles [13] in an incompressible liquid. He used a free surface approach to model vapour bubbles and studied the effect that viscosity has on the formation of jets during bubble collapse. A combined level set and VOF method (CLSVOF) was developed by Sussman [14], which was shown to have second order convergence in space and time. Can and Prosperetti [15] used a level set method and studied the evolution of a vapour bubble in a microtube.

A DNS study of the propagation of shock waves in an incompressible liquid containing multiple compressible gas bubbles was performed by Delale et al. [16] using front tracking to capture the liquid-vapour interface. In terms of high performance computing,

Rossinelli et al. [17] performed a very large simulation on the collapse of vapour bubbles. A computational mesh of 13×10^{12} grid points was used to simulate the collapse of around 15000 bubbles. This was a study focussing on high performance computing aspects of CFD and, however impressive it was, it presented very limited results of the flow physics and the details of the boundary conditions were not mentioned. Additionally, no capillary effects were included in the governing equations.

This study will similarly use a free surface approach to model multiple, compressible bubbles in an incompressible carrier liquid. It will use a VOF method, coupled with the PLIC interface representation to study, for the first time in our estimation, the capillary effects on bubble clouds in a liquid under tension using Detailed Numerical Simulation.

2. Mathematical formulation

We solve the flow in an incompressible, inviscid liquid with a sharp interface of arbitrary shape to a gas phase. We assume this interface moves freely and apply a Dirichlet boundary condition for the pressure at the interface. This pressure value is computed using the gas phase pressure as well as the pressure jump due to surface tension. The liquid flow is then governed by the incompressible Euler equations.

Momentum conservation in the liquid is described by

$$\frac{\partial \mathbf{u}}{\partial t} + \mathbf{u} \cdot \nabla \mathbf{u} = -\frac{\nabla p}{\rho}, \quad (2)$$

with ρ and \mathbf{u} respectively the liquid density and velocity, while p is the pressure inside the liquid. Note that the surface tension term is excluded here, but is accounted for in the pressure boundary condition at the free surface.

For the incompressible liquid phase, mass conservation is given by

$$\nabla \cdot \mathbf{u} = 0. \quad (3)$$

The pressure of the unresolved phase can be determined from an equation of state. In this case adiabatic conditions are assumed and a polytropic gas law is applied [18] to compute the gas pressure in the cavity

$$p_c = p_0 \left(\frac{V_0}{V_c} \right)^\gamma, \quad (4)$$

where V_c is the total volume of a single gas cavity at pressure p_c , p_0 and V_0 are respectively the reference pressure and volume of the gas phase, γ is the heat capacity ratio.

The pressure at the free surface on the liquid side, p_s , is equal to the gas pressure with the addition of the Laplace pressure jump due to surface tension

$$p_s = p_c + \sigma \kappa, \quad (5)$$

where σ is the surface tension coefficient, here assumed to be constant. The interface curvature is given by κ . The interface is captured using a Volume-Of-Fluid (VOF) [19] method. The VOF method defines a colour function, c , in each control volume, which represents the volume fraction of the reference phase present in that particular volume. For a control volume V_ℓ , c is then given by

$$c = \frac{1}{|V_\ell|} \int_{V_\ell} H(\mathbf{x}, t) dV \quad (6)$$

where $H(\mathbf{x}, t)$ is the Heaviside function, satisfying $H = 1$ inside the carrier phase and $H = 0$ outside it.

The evolution of the color function is governed by the following advection equation, which is intended to be solved in a weak form by integrating over finite volumes

$$\frac{\partial c}{\partial t} + \mathbf{u} \cdot \nabla c = 0. \quad (7)$$

3. Numerical method

The governing equations are discretized on an equi-spaced Cartesian mesh in the so-called MAC arrangement [20]. Volume-averaged scalar values (p and c) are located in the center of computational cells, while scalar components of velocity are located on cell faces. The liquid density is considered constant.

3.1. Time integration

The above system of equations is solved numerically using a projection method [21]. The discrete form of the equations that follow are written for an explicit first order time integration to illustrate the numerical procedure. First, a temporary velocity field \mathbf{u}^* is obtained by solving

$$\frac{\mathbf{u}^* - \mathbf{u}^n}{\Delta t} = -\mathbf{u}^n \cdot \nabla^h \mathbf{u}^n \quad (8)$$

where Δt is the time step, the superscript n refers to the n th time step and ∇^h is the discrete gradient operator. The velocity at the next time step, $n + 1$, is then obtained by adding the contribution of the pressure term

$$\frac{\mathbf{u}^{n+1} - \mathbf{u}^*}{\Delta t} = -\frac{\nabla^h p^{n+1}}{\rho}. \quad (9)$$

The pressure gradient will be calculated to include surface tension at the interface. This will be detailed in Section 3.2. For incompressibility of the flow we require

$$\nabla^h \cdot \mathbf{u}^{n+1} = 0, \quad (10)$$

and by substituting (9) in (10) we have

$$\nabla^h \cdot \left[\frac{\Delta t}{\rho} \nabla^h p^{n+1} \right] = \nabla^h \cdot \mathbf{u}^*. \quad (11)$$

We therefore find the divergence-free velocity field at time step $n + 1$ by correcting the temporary velocity field \mathbf{u}^* with the pressure found by solving (11) and then using (9)

$$\mathbf{u}^{n+1} = \mathbf{u}^* - \frac{\Delta t}{\rho} \nabla^h p^{n+1}. \quad (12)$$

These equations are solved for the liquid flow. We have an arbitrary, free surface interface to the gas phase and track the liquid using a VOF method, for which we solve an advection equation, which includes the divergence-free condition (3)

$$c^{n+1} = c^n - \Delta t [\nabla^h \cdot (c \mathbf{u})^n]. \quad (13)$$

This equation is solved in two steps: reconstruction of the interface as a plane in each grid cell and then its advection with the computation of the reference phase fluxes across the cell boundary. The use of planes to reconstruct the interface is sometimes referred to as piecewise linear interface construction (PLIC) and is accredited to De Bar [22]. In the first part of the reconstruction step, the interface normal \mathbf{n}_s is computed with the “mixed Youngs-centered” (MYC) method [23]. Then the position of a plane, representing the interface in the cell, is determined using elementary geometry [24]

$$\mathbf{n}_s \cdot \mathbf{x} = n_{sx}x + n_{sy}y + n_{sz}z = \alpha, \quad (14)$$

where the scalar α characterizes the position of the interface. For the computation of the reference phase fluxes we can use the Lagrangian explicit CIAM scheme [25] or the strictly conservative Eulerian scheme of Weymouth and Yue [26].

A well-known method [14,27] to increase the convergence order of time integration is to calculate two explicit time steps and then halve the result

$$\tilde{\mathbf{u}}^* = \mathbf{u}^n + \Delta t L(\mathbf{u}^n) \quad (15)$$

$$\mathbf{u}^{**} = \tilde{\mathbf{u}}^* + \Delta t L(\tilde{\mathbf{u}}^*) \quad (16)$$

$$\mathbf{u}^* = \frac{1}{2}(\mathbf{u}^{**} + \mathbf{u}^n), \quad (17)$$

where $\tilde{\mathbf{u}}^*$ is an intermediate temporary velocity field and L is the advection operator of (8).

3.2. Treatment at the free surface

At the interface to the gas phase, a Dirichlet boundary condition for the pressure needs to be applied to include the effects of the cavity pressure and surface tension on the liquid flow. The method used in this work is inspired by the idea of Fedkiw and Kang [28,29], often referred to as the ghost fluid method. First, the pressure in each individual cavity is found from (4). In this equation, p_0 and V_0 are known gas quantities, but the volume V needs to be calculated for each individual cavity.

An algorithm was previously added into PARIS by Yue Ling which is capable of identifying continuous volumes of a tracked phase (in our case gas) inside the domain. This algorithm is based on Herrmann's [30] and makes use of the color function c . The first step is to loop through the entire computational domain, check whether a cell contains the tracked phase and tag it. Neighboring cells will be assigned the same tag number. The next step is to agglomerate continuous volumes of the tracked phase across processor boundaries for parallel computations. The output of the algorithm is a lookup table for each agglomerated volume, containing its volume, centroid location, velocity and other information. This lookup table is interrogated to obtain the volume V for each cavity, which in turn allows for the calculation of p_c using (4).

With the value of p_c calculated for each cavity, special care is required in the discretization of (11) for liquid cells near the interface. Cells that contain mostly gas are excluded from the solution, so that only cells where $c < 0.5$ are solved (with $c = 0$ in the liquid).

Fig. 2 shows a representation of a 2D grid with a section of an interface. The grey area represent a vapour-filled cavity. Cells that contain a filled circle are included in the pressure solution, while

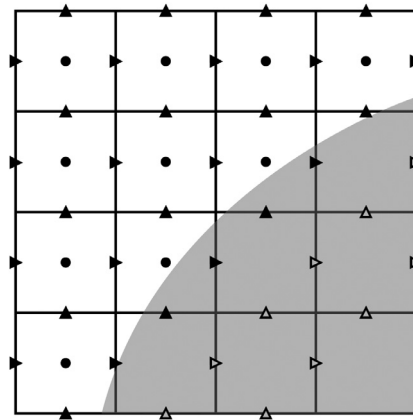
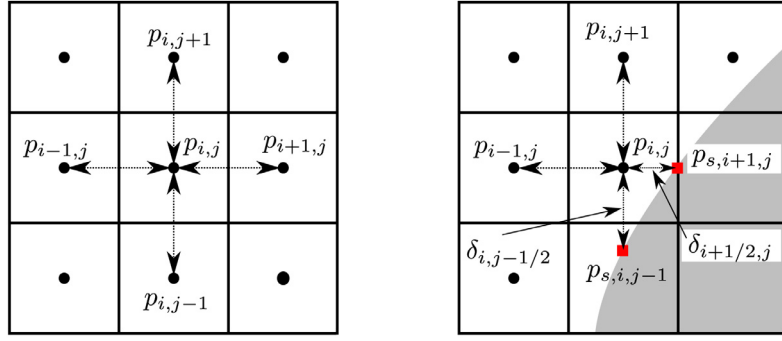


Fig. 2. A portion of the 2D computational mesh, showing part of a gas bubble in grey. Filled circles represent the cell nodes where pressure is calculated. Triangles indicate scalar velocity components on the computational cell face: filled triangles indicate values which are found by solving the governing equations, while empty triangles represent boundary values found by extrapolation.



(a) Standard discretisation of the pressure equation in the liquid bulk

(b) Discretisation of the pressure equation near the interface

Fig. 3. Schematic representation of the Poisson equation discretisation.

cells without a marker are excluded. The finite volume discretisation of the left hand side of (11) for a bulk liquid cell in 2D, shown in Fig. 3a, is written as

$$\begin{aligned} \frac{\Delta t}{|V_{i,j}|} \int_{V_{i,j}} \nabla \cdot \left[\frac{\nabla^h p^{n+1}}{\rho} \right] dV \\ \approx \frac{\Delta t}{\rho} \left(\frac{\nabla_y^h p_{i,j+1/2} - \nabla_y^h p_{i,j-1/2}}{\Delta y} + \frac{\nabla_x^h p_{i+1/2,j} - \nabla_x^h p_{i-1/2,j}}{\Delta x} \right) \\ = \frac{\Delta t}{\rho} \frac{p_{i,j+1} + p_{i,j-1} + p_{i+1,j} + p_{i-1,j} - 4p_{i,j}}{h^2}, \end{aligned} \quad (18)$$

where the i and j subscripts are integer indices for the discrete computational cell with volume $V_{i,j}$. Since the equation above is only applied in the liquid phase and thermal effects are neglected, then the density ρ is assumed constant. Furthermore, for cubic cells $\Delta x = \Delta y = \Delta z = h$, where h is the constant grid spacing.

The stencil for the pressure gradient components has to be changed near the interface when a neighbouring pressure in expression (18) falls inside the gas phase. This point must be disregarded and its pressure substituted by a surface pressure. We apply the same approach as Chan's [31]. As an example, the approximation for the pressure gradient components for the cell with indices i and j in Fig. 3b is written

$$\nabla_x^h p_{i+1/2,j} = \frac{p_{s,i+1,j} - p_{i,j}}{\delta_{i+1/2,j}}; \quad \nabla_y^h p_{i,j-1/2} = \frac{p_{i,j} - p_{s,i,j-1}}{\delta_{i,j-1/2}}, \quad (19)$$

where δ is the length of the segment connecting the pressure node under consideration and the intersection with the interface along the relevant coordinate direction. The pressure p_s on the liquid side of the interface is found by adding to p_c the Laplace pressure jump. The gas pressure p_c inside each cavity is known from (4). The interface pressure in the x -direction will then be

$$p_{s,i+1,j} = p_{c,i+1,j} + \sigma \frac{\kappa_{i,j} + \kappa_{i+1,j}}{2}. \quad (20)$$

From (20) and (19) it is clear that accurate estimates of both the interface curvature as well as the interface position are important parameters to ensure the accuracy of the pressure solution.

The interface curvature is computed with the height function method [32]. The height function defines the approximate position of a point on the interface with respect to a reference cell face [33], and is calculated by summing the VOF values in a column of grid cells, called a height stack, which is aligned with the Cartesian direction perpendicular to the cell face. The principal curvature can

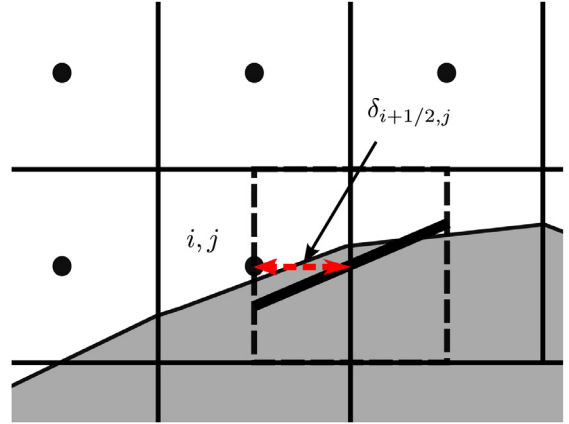


Fig. 4. With the given interface configuration, cell i, j will typically have a vertical height column, but not a horizontal one. A plane reconstruction (thick black line) is made in the staggered volume indicated with dashed lines and this reconstruction is used to obtain $\delta_{i+1/2,j}$.

then be obtained by using finite difference approximations for the first and second derivatives of the height function. This method has been shown to produce second-order accuracy for the curvature [34].

It is not always possible to find all the required heights to calculate a curvature. In this case a paraboloid is fitted through the plane centroids of neighbouring interface cells, and then is used to estimate the curvature.

The length δ in the pressure gradient components (19) near the interface can also be easily calculated if the height function is defined along the relevant coordinate direction. In Fig. 3b the length $\delta_{i+1/2,j}$ is given by the absolute value of the difference between the local horizontal height (red point on the right of Fig. 3b), and the abscissa of the midpoint of cell i, j , both measured from the same reference cell. When the interface configuration is such that a local height cannot be obtained in the required direction, the length δ is then approximated by using a plane reconstruction of the interface in the staggered volume, as shown in Fig. 4.

First, the staggered VOF fractions are obtained by considering the plane reconstruction in centered cells and by computing and adding the half fractions of Fig. 4. A procedure similar to that of centered cells is then used in the staggered cells to reconstruct the interface as a plane, as in (14). Once the plane equation is known, the interface distance $\delta_{i+1/2,j}$ can then be easily calculated.

The finite difference discretization of the left hand side of (11) for cell i, j in Fig. 3b will then be

$$\begin{aligned} \frac{\Delta t}{\rho} \nabla^h \cdot [\nabla^h p^{n+1}] &\approx \frac{\Delta t}{\rho} \left(\frac{\nabla_y^h p_{i,j+1/2} - \nabla_y^h p_{i,j-1/2}}{1/2(\Delta y_{j+1/2} + \Delta y_{j-1/2})} + \frac{\nabla_x^h p_{i+1/2,j} - \nabla_x^h p_{i-1/2,j}}{1/2(\Delta x_{i+1/2} + \Delta x_{i-1/2})} \right) \\ &= \frac{\Delta t}{\rho} \left(\frac{2}{h + \delta_{i,j-1/2}} \left(\frac{p_{i,j+1} - p_{i,j}}{h} - \frac{p_{i,j} - p_{s,i,j-1}}{\delta_{i,j-1/2}} \right) \right. \\ &\quad \left. + \frac{2}{\delta_{i+1/2,j} + h} \left(\frac{p_{s,i+1,j} - p_{i,j}}{\delta_{i+1/2,j}} - \frac{p_{i,j} - p_{i-1,j}}{h} \right) \right). \end{aligned} \quad (21)$$

The implementation in 3D is included in PARIS.

3.3. Extrapolation of the velocity field

The previous section dealt mainly with the discretisation of the pressure term near the interface. The solution of the Poisson equation (11) for the pressure is used in (12) to correct the temporary velocity field \mathbf{u}^* obtained in (8). This section will deal with the extrapolation of the velocity field, which is required in the advection term on the right hand side of (8). The advection term $\mathbf{u} \cdot \nabla \mathbf{u}$ can be discretized using a choice of schemes, including QUICK [35], ENO [36] and WENO [37].

For all these schemes, the discretization of $\mathbf{u} \cdot \nabla \mathbf{u}$ may require a velocity stencil including neighbours up to two grid spacings away, depending on the upwind direction. The discrete pressure nodes that are included in the solution have been discussed in the previous section, and we need to do the same for the velocity components, considering also the fact that we are on a staggered grid. The velocity components that have to be included in the solution of the governing equations are all those on the boundary of the grid cells where the pressure is computed. These velocity components are marked with filled triangles in Fig. 2. We recall that in a staggered MAC discretisation on each cell face is located only the normal component of the velocity.

As mentioned earlier, the resolved velocity components right next to the interface will require neighbours in the gas phase in order to discretize the advection term in the momentum equation with an upwind scheme. These values in the gas phase can be considered as boundary values to the resolved velocity components. In order to find neighbours in the gas phase, we extrapolate the resolved velocities similarly to Popinet's [34].

After calculating \mathbf{u}^{n+1} in (9), we have a field of updated velocities in the liquid. To find the boundary velocities for the next time step, the closest two neighbours of each velocity component are extrapolated from the field of liquid velocities using a linear least square fit. Let's assume that the velocity field near a point \mathbf{x}_0 with extrapolated velocity \mathbf{u}_0 can be approximated by the linear expression

$$\mathbf{u}(\mathbf{x}) = \mathbf{A}_0 \cdot (\mathbf{x} - \mathbf{x}_0) + \mathbf{u}_0 \quad (22)$$

where the components of the tensor $\mathbf{A}_0 = \nabla \mathbf{u}_0$ and of the vector \mathbf{u}_0 are the unknowns.

If we now take a 5×5 stencil around the unknown gas velocity at location \mathbf{x}_0 , we can find the extrapolated velocity \mathbf{u}_0 by minimizing the functional

$$\mathcal{L} = \sum_{k=1}^N |\mathbf{A}_0 \cdot (\mathbf{x}_k - \mathbf{x}_0) + \mathbf{u}_0 - \mathbf{u}_k|^2 \quad (23)$$

This is done first for all locations closest to the resolved velocities \mathbf{u}_k ("first neighbours"), whereafter the process is repeated for

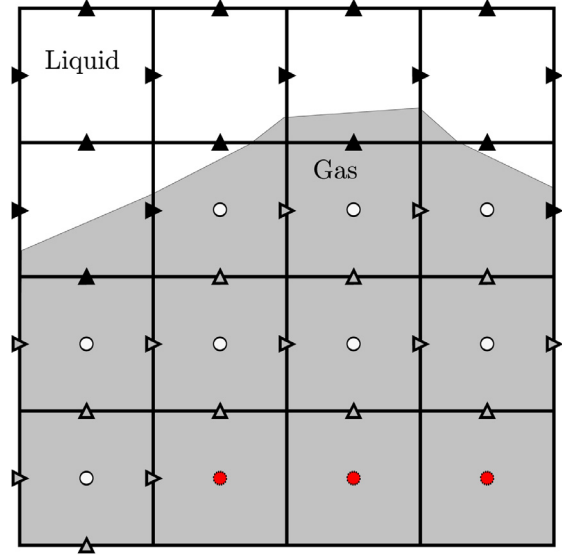


Fig. 5. 2D example of the problem to correct the extrapolated velocities (unfilled triangles). A Poisson problem is solved in the cells marked with an unfilled circle.

the "second neighbours". Note that only resolved velocity components are included in the cost function, therefore the number N of resolved velocities can vary depending on the shape of the interface. Furthermore, because of the staggered grid, only one velocity component of \mathbf{u}_0 is computed at location \mathbf{x}_0 .

3.4. Ensuring volume conservation

After the liquid velocities have been extrapolated into the gas phase, an additional step is required to ensure that these velocities are divergence free. This is required to ensure that the advection of the colour function (7) is conservative.

An approach similar to Sussman's [14] is used. Only the first two layers of cells inside the gas phase are considered and all other cells are disregarded. A 2D example is presented in Fig. 5. A "phantom" pressure is computed in the cells with extrapolated velocity components in all its faces, by solving the following Poisson equation, which is close to that of the projection step (11) previously discussed,

$$\nabla^h \cdot (\nabla^h \hat{P}) = \nabla^h \cdot \mathbf{u}_0, \quad (24)$$

where \hat{P} is the "phantom" pressure and \mathbf{u}_0 is the extrapolated velocity on the faces of the first two gas neighbours. \hat{P} must be calculated only in the cells represented by unfilled nodes in Fig. 5. On the liquid side of these cells, the solved velocities (filled triangles) are used as a velocity boundary condition with the pressure gradient on this face set to zero. On the gas side, beyond the cells where the pressure \hat{P} is computed, a fixed pressure is prescribed (red filled circles). Only the extrapolated velocities (unfilled triangles) are then corrected by the solved pressure gradient $\nabla \hat{P}$

$$\mathbf{u}_0^{n+1} = \mathbf{u}_0 - \nabla^h \hat{P}, \quad (25)$$

to ensure a divergence-free velocity field in the first two layers of cells just inside the gas.

4. Results

4.1. Single bubble validation with Rayleigh-Plesset equation

A widely-used [13–15] validation test for volume-changing bubbles in an incompressible liquid, is to compare a numerical simulation of a single gas bubble with a fixed liquid pressure at infinity

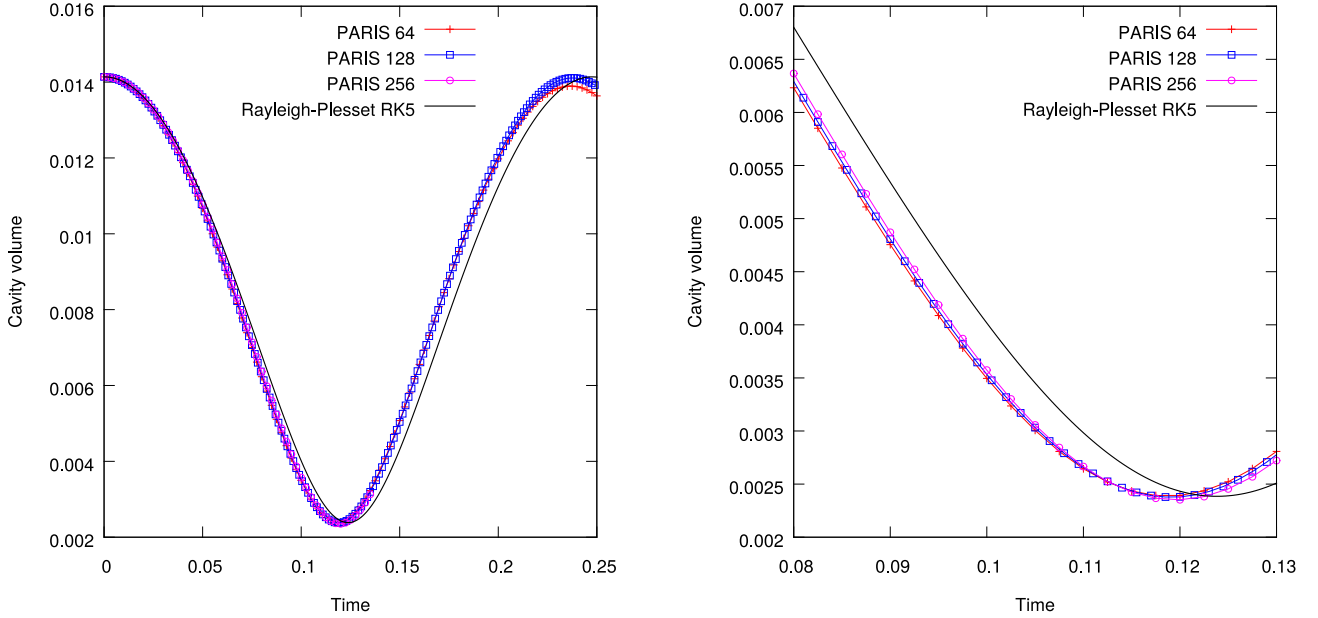


Fig. 6. Comparison between PARIS simulations and the solution of the Rayleigh-Plesset equation for the time evolution of the volume of a single oscillating gas bubble at different grid resolutions $h = 1/N$, $N = 64, 128, 256$ of the unit cube, $L = 1$. Simulation of a complete oscillation (left) and local zoom near the minimum (right).

to the solution of the Rayleigh-Plesset equation [38]. This equation describes the evolution of a bubble of radius R in an incompressible liquid, assuming spherical symmetry with some fixed pressure at infinity. A derivation of this equation is given in Appendix A. Neglecting viscous effects, the Rayleigh-Plesset equation is written for the evolution of the radius R of a gas bubble, exposed to a pressure p_∞ at infinity

$$\ddot{R} + \frac{3}{2}\dot{R}^2 = \frac{p_s - p_\infty}{\rho_l} = \frac{p_c - 2\sigma/R - p_\infty}{\rho_l} \quad (26)$$

where R is the bubble radius, p_s the pressure on the liquid side of the interface, p_∞ the pressure at infinity, σ the surface tension coefficient and ρ_l the liquid density. The bubble pressure, p_c , is obtained from a polytropic gas law

$$p_c(t) = p_0 \left(\frac{V_0}{V(t)} \right)^\gamma \quad (27)$$

where $\gamma = 1.4$ is the isentropic gas coefficient, V_0 is the bubble volume at some reference pressure p_0 and $V(t)$ is the bubble volume.

4.1.1. Simulation setup

A bubble of radius R is placed in the center of a cubic domain, with side $L = 1$. The initial bubble radius is chosen such that the bubble is not in equilibrium with p_∞ and will expand or shrink as a result.

The application of boundary conditions to the problem is not trivial, since some finite sized flow domain must be created, while the Rayleigh-Plesset equation is derived with a pressure at an infinite distance. This problem is addressed by using the solution of (26) to obtain an expression for the pressure

$$p(r, t) = p_s - \rho_l \left(\frac{\dot{R}^2 R^4}{2r^4} - \frac{\ddot{R} R^2 + 2R\dot{R}^2}{r} + \ddot{R}R + \frac{3}{2}\dot{R}^2 \right). \quad (28)$$

The derivation is given in the Appendix. The solution for the Rayleigh-Plesset equation (26) is obtained numerically with a fifth order Runge-Kutta integration method. The time step size for the

numerical solution of (26) is deliberately chosen to coincide with that of the PARIS simulation, to ensure that the pressure calculated from (28) is applied consistently at the boundary. A zero normal gradient is applied for the velocity on the boundary.

A test case is set up with the following parameters: a bubble with initial radius $R(t=0) = 0.15$ is placed in the center of a cubic domain, containing liquid with density $\rho_l = 1.0$ and a surface tension coefficient $\sigma = 0.05$. The bubble is assumed to be initially at rest, $\dot{R}(t=0) = 0$. The bubble has a radius $R_0 = 0.14$ at the reference pressure $p_0 = 1.0$, while the pressure at infinity is $p_\infty = 1.5$.

First, a time convergence study was performed to determine a fixed time step size. The solution was found to be suitably converged in time for a time step of $\Delta t = 10^{-5}$, or smaller, on a grid with $N_x \times N_y \times N_z = 64^3$ grid points.

Three simulations were completed for one oscillation cycle with 64^3 , 128^3 and 256^3 grid points and time step sizes $\Delta t = 10^{-5}$, $\Delta t = 5 \times 10^{-6}$ and $\Delta t = 2.5 \times 10^{-6}$ respectively.

Fig. 6 shows a comparison between the results in PARIS and a numerical solution of the Rayleigh-Plesset equation. In Table 1, some quantitative results are given. More specifically, the cavity volume at time $t=0.075$ is compared to the theoretical volume computed by the numerical solution of (26) and the relative error is calculated. The time at which the cavity reaches its minimum volume is also compared to the theoretical value.

A relatively good agreement was achieved, but the rate of convergence in space is slow, which may suggest that the PARIS simulations are close to being converged in space. Another important factor to be considered in this test case, is the boundary effect which is caused by applying a zero normal gradient to the velocity on the cube boundary, while the actual velocity field is spherically symmetric. One way to compensate for this effect is to increase the ratio L/\bar{R} , between the domain length L and the mean bubble radius \bar{R} . To study this effect, the same test case was considered, but with varying domain sizes L . Three cases were tested, with $L = 0.5$, $L = 1.0$ and $L = 2.0$, respectively, while both the grid spacing ($h = 1/128 \approx 7.813 \times 10^{-3}$) and the time step size ($\Delta t = 5 \times 10^{-6}$) are kept constant. The results are shown in Fig. 7 and the relative errors, for the same conditions of Table 1, are presented in Table 2.

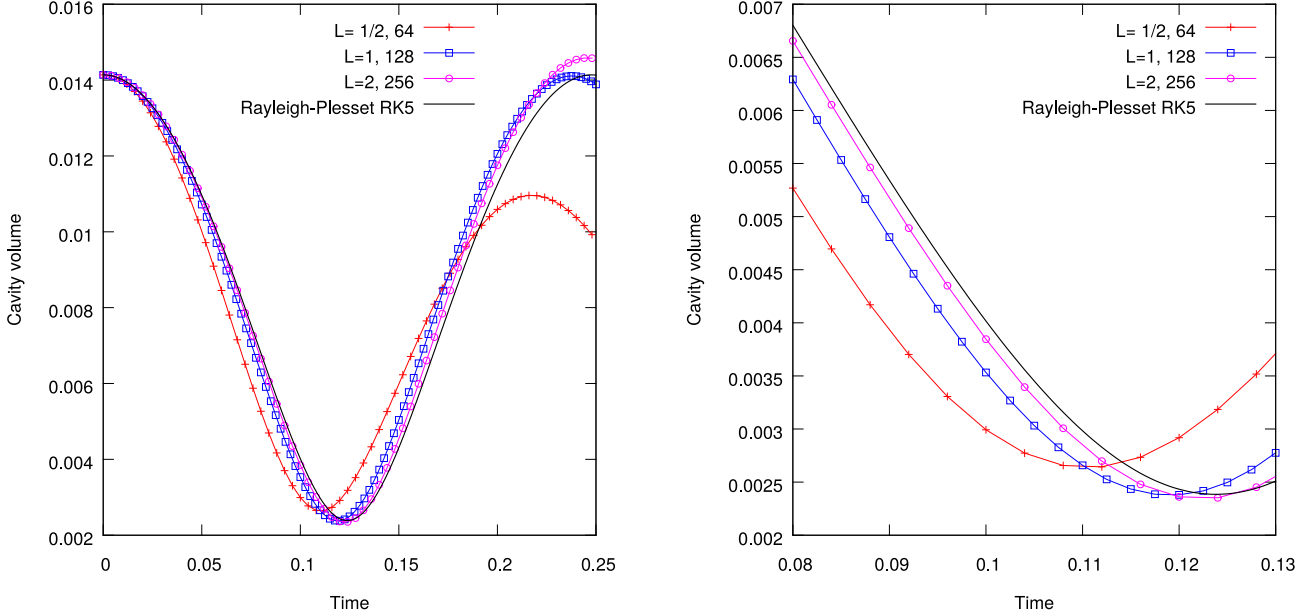


Fig. 7. Results of the same test case of Fig. 6, but for three different cube sides, $L = 1/2, 1, 2$, and constant h and Δt .

Table 1

The cavity volume at $t = 0.075$ is compared to the theoretical value (7.5446×10^{-3}) for three different grid resolutions. The time at which the volume reaches a minimum is also compared to the theoretical value (0.124).

Cell size, h [$\times 10^{-3}$]	Vol., $t = 0.075$ [$\times 10^{-3}$]	Vol. Error [%]	t at V_{\min}	t Error [%]
15.63	7.004	7.16	0.1187	4.27
7.813	7.065	6.35	0.1191	3.95
3.906	7.141	5.35	0.1195	3.63

Table 2

The relative errors are calculated using the same criteria as in Table 1, but for three different ratios of L/R .

L/R ratio	Vol., $t = 0.075$ [$\times 10^{-3}$]	Vol. Error [%]	t at V_{\min}	t Error [%]
4.29	6.032	20.05	0.1105	10.89
8.59	7.065	6.35	0.1191	3.95
17.18	7.411	1.77	0.1225	1.21

It can be seen from these results that the solution in Fig. 6 likely suffered from the boundary effect. To further investigate this point, another test was created with the initial radius of the bubble $R(t = 0) = 0.10$. The remaining parameters are selected such that the bubble radius decreases significantly more than in the previous test, thereby ensuring that the ratio L/R is much higher. The surface tension is $\sigma = 0.10$, $p_\infty = 0.5$ and the reference pressure is $p_0 = 1.0$ at a radius $R_0 = 0.9$. This final test case was run on a domain with $L = 1.0$ with 128^3 grid points. The results for two complete bubble oscillations are shown in Fig. 8.

A much better agreement is now obtained between the 3D results of PARIS and the numerical integration of the Rayleigh-Plesset equation. Note that the grid resolution in this problem is again $h = 1/128$, and this fact gives confidence that a large portion of the error is indeed attributable to the boundary effect. Further convergence studies become prohibitively expensive without the use of adaptive mesh refinement. However, the agreement achieved in this test problem is considered sufficient to proceed with the study of the model problem.

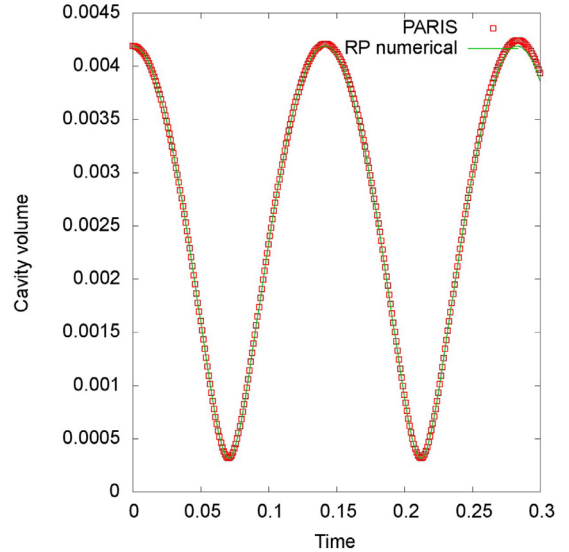


Fig. 8. Comparison between the PARIS simulation and the solution of the Rayleigh-Plesset equation with $L = 1$ and $h = 1/128$, but smaller initial radius of the bubble and slightly different physical parameters than the test case of Fig. 6.

4.2. Multiple bubble tests

In this section the results of model problem simulations containing multiple pre-nucleated bubbles are presented. The setup of the numerical simulations will be described and some non-dimensional numbers will be defined by which the flow can be characterized. A parametric study will then be performed.

4.2.1. Simulation setup

As mentioned in the introduction, the shock wave effect in the liquid will be modelled with a constant rate of expansion, ω . This is imposed by applying a constant outflow velocity, U_n , normal to all faces of the cubic domain, so that

$$\omega = \frac{6U_n}{L}, \quad (29)$$

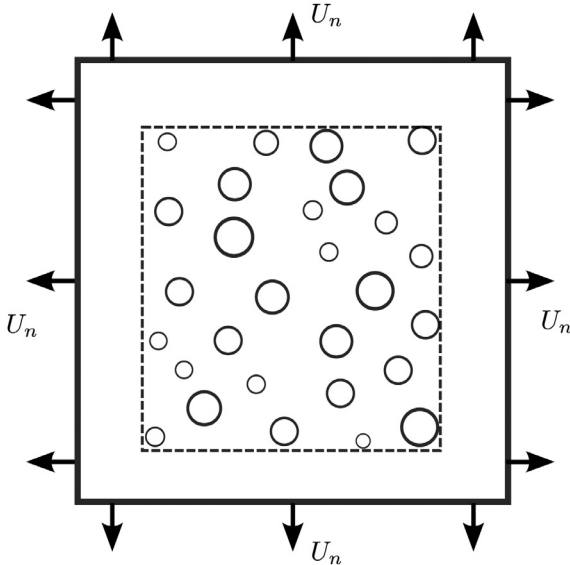


Fig. 9. 2D slice through domain showing a typical simulation setup. A uniform velocity outflow rate is specified on the domain faces. Bubbles are initialised in an internal bubble zone, surrounded by a layer of pure liquid.

with $L = 1$ the length of the cube. This boundary condition fixes the growth rate of the void fraction, since the liquid is assumed incompressible. Another possible approach could be to fix the boundary pressure. Both options yield a kind of "equation of state". Whereas imposing velocity is physically more unstable (the pressure resulting from an imposed velocity may have spikes as in the waterhammer effect), imposing the velocity is numerically more convenient and stable, (outflow conditions can be tricky). Since our system is intrinsically unstable anyway (the speed of sound is imaginary) it seemed preferable to use the velocity condition.

All simulations are started with bubbles pre-nucleated at some finite size. Bubbles are seeded in a face centered cubic (FCC) lattice. The bubble positions can correspond to the exact lattice nodes, or with some random displacement around this position. Fig. 9 shows

a 2D slice of a typical simulation setup. Bubbles are placed in a central zone, referred to as the bubble zone. An all-liquid zone along the boundary of the computational domain forms a liquid layer between the bubbles and the outflow faces. The size of this zone is chosen such that only liquid exits the domain up to a void fraction of approximately 30%. The inter-bubble distance, ℓ_D , is given by

$$\ell_D = \left(\frac{L^3}{N_0} \right)^{\frac{1}{3}}, \quad (30)$$

with N_0 the number of pre-nucleated bubbles. Bubbles are initialized with a variable radius R_0 and the parameter $\Delta R_0/R_{\min}$ describes the variance in the initial bubble diameter, so that $R_{\min} < R_0 < R_{\min} + \Delta R_0$. Once the center position and radius of each bubble have been generated, the initial conditions for the colour function can be easily and accurately initialized with the VOF library [39,40]. An advantage observed when using this library is a significant drop in computational time compared to iterative, mesh refinement techniques to generate the initial field.

To further characterize the problem, a Weber number is introduced based on the fluid density ρ , surface tension σ and the inter-bubble distance defined above

$$We = \frac{\rho \ell_D^3 \omega^2}{\sigma}. \quad (31)$$

Considering the Weber number, two extreme limits of flow type exist. In the $We \rightarrow 0$ limit, when $U_n \rightarrow 0$ or $\sigma \rightarrow \infty$, surface tension dominates over expansion. In the opposite case, the expansion dominates over surface tension when $U_n \rightarrow \infty$ or $\sigma \rightarrow 0$ and $We \rightarrow \infty$. This situation can be thought of as bubbles that have some finite size and are driven to expand by a large fluid expansion rate and surface tension effects are overpowered by strong inertial pull of the rapidly expanding fluid. In this case we would expect that all cavities grow at close to the same rate and ultimately percolate.

First, the $We = 0$ limit is studied and then some cases with increasing We will be presented. As the Weber number is increased, we are mainly interested in the individual bubble evolution. With the given boundary conditions, we know the growth rate of the

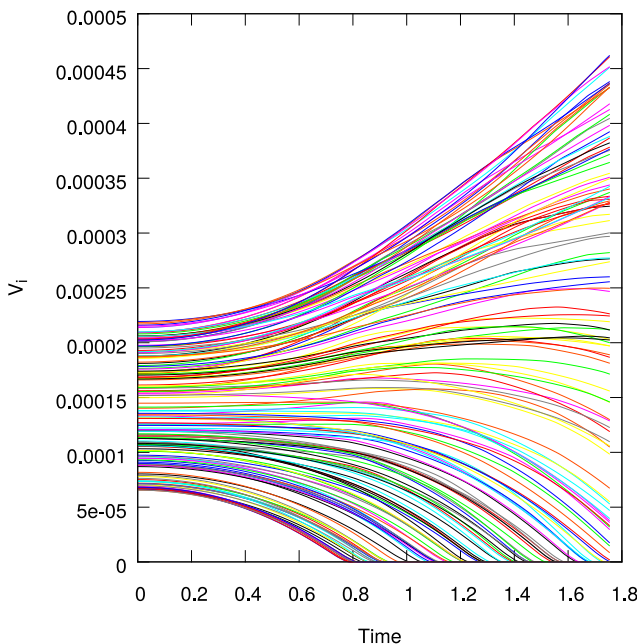


Fig. 10. Time evolution of the volume of the bubbles for the $We = 0$ case. On the right a logarithmic plot is presented in which the time is re-scaled by τ_R .

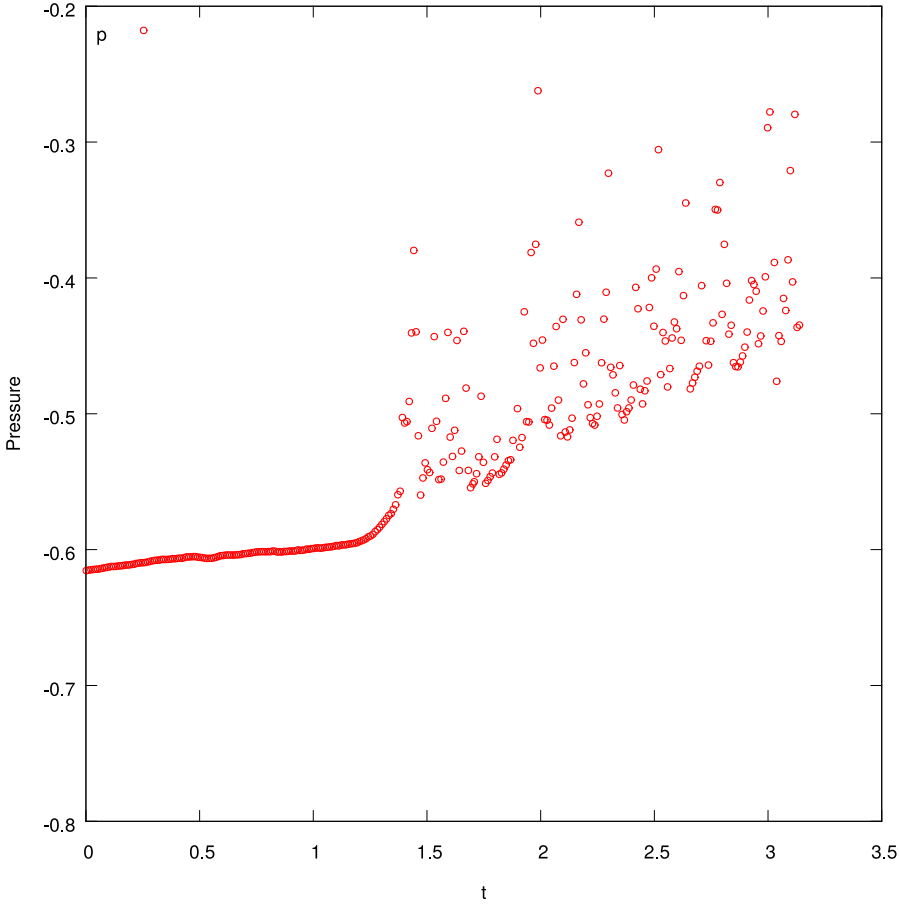


Fig. 11. The average pressure in the domain for the $We = 0$ case. Note that the negative pressures are not of concern, as the actual value does not have a meaning in incompressible flow. The reason for the negative values is the zero vapour pressure in cavities.

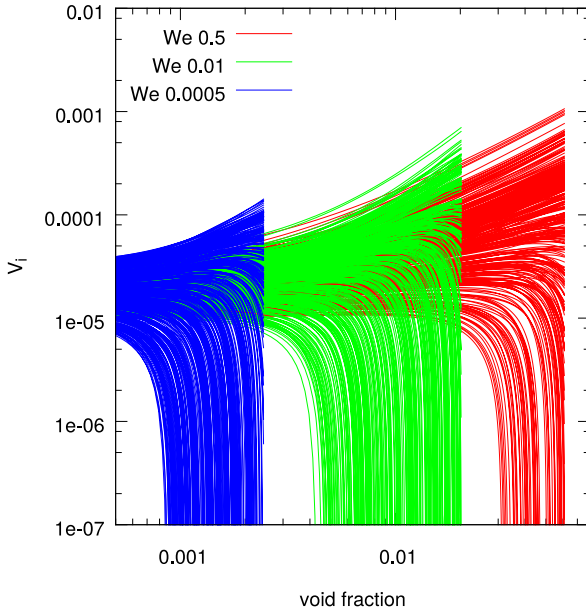


Fig. 12. Comparison of individual bubble volumes for varying We . Bubble collapse is delayed with increasing We as the domain expansion counters capillary effects. Individual bubble volumes are plotted as function of total void fraction.

void fraction, but we do not know in advance how individual bubbles will evolve to achieve this void fraction and what the influence of We on this process is. More particularly, even though the

Table 3
Simulation parameters for multiple bubble tests.

Parameter	Value
Liquid buffer to domain length ratio	0.12
Expansion rate ω	0.033, 0.165, 1.05
Initial bubbles N_0	365
Grid points	512 ³
We	$5 \cdot 10^{-4}$, 0.013, 0.54
$\Delta R_0/R_{\min}$	0.5
$\Delta \ell_D/\ell_D$	0, 0.2

growth rate of the total bubble volume is given, each single bubble may evolve differently from the expected mean growth rate and this fact affects the total surface area of the bubbles in the domain and therefore the total surface energy.

4.2.2. Zero Weber

A test case is presented for $We \rightarrow 0$. This case is created by defining a simulation where periodic boundary conditions are used on a unit cube, instead of using an outflow velocity U_n . There are 172 bubbles pre nucleated with $R_{\min} = 0.025$ and $\Delta R_0/R_{\min} = 0.5$. The bubble zone is an inner cube with length 0.75.

The time evolution of the volume of the bubbles is shown in Fig. 10. The bubbles are initialized with a random size distribution, as can be seen at time zero. In this case there is no net flux from the domain, so the void fraction remains constant throughout the simulation. However, the individual bubbles either grow or shrink. This can be seen as a surface energy minimization process in which the system grows some bubbles (in general larger ones),

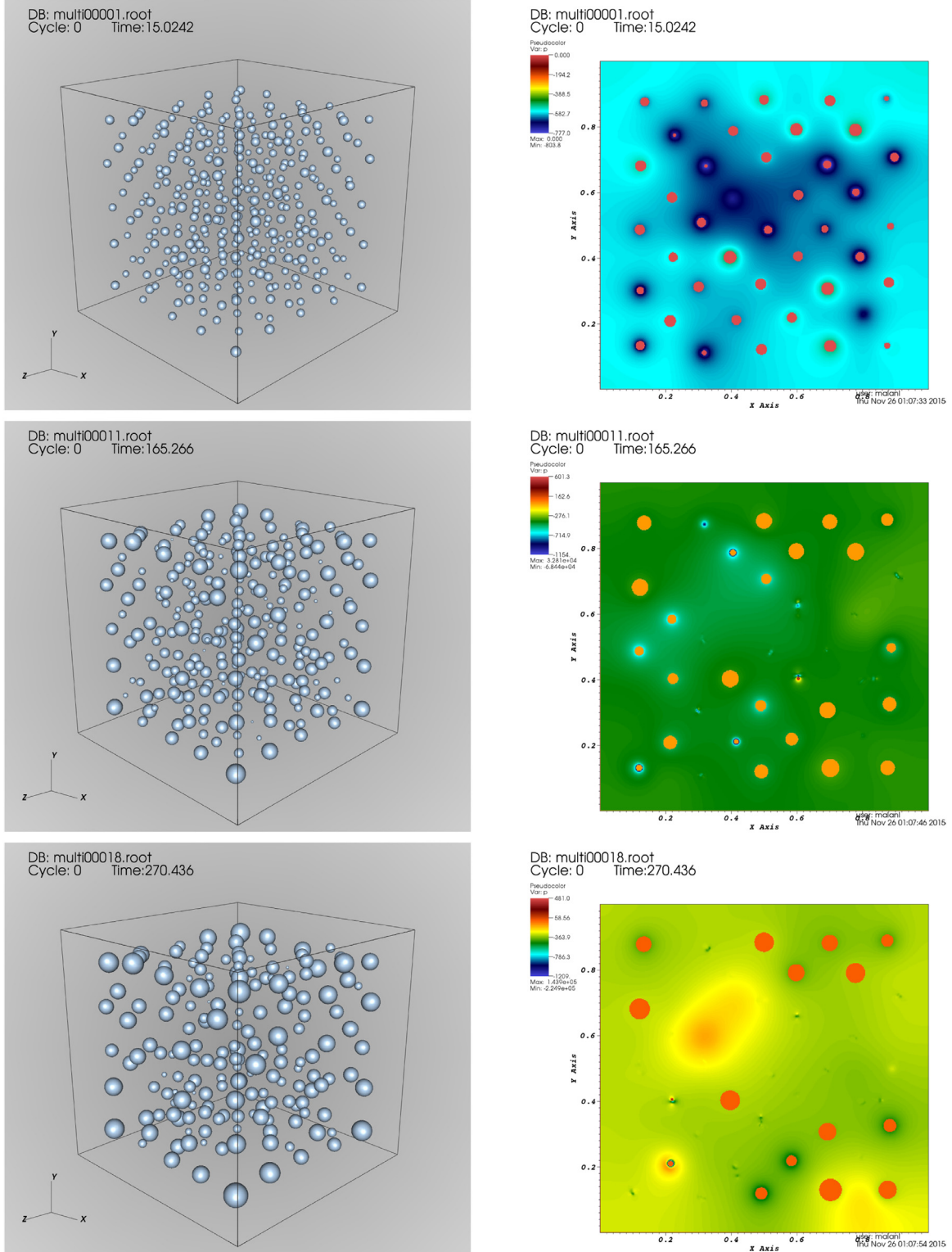


Fig. 13. Visit screenshots of a simulation with 365 initial bubbles at $We = 0.1$. The left column shows a 3D view of the bubbles population at progressive time steps. The images on the right show the pressure distribution at the same instances on a section at $z = 0.5$.

while some shrink. We can also define a time scale τ_R based on the bubble radius and fluid parameters

$$\tau_R = \left(\frac{\rho R^3}{\sigma} \right)^{\frac{1}{2}}, \quad (32)$$

with $\rho = 1000$ and $\sigma = 0.01$ in this case. It is then clear from the plot on the right of Fig. 10 that this time scale is the time scale of bubble collapse.

A plot of the pressure in Fig. 11 shows how the average pressure evolves in the domain. The increase in pressure is indicative of the tension in the system relaxing. The negative value of pressure is

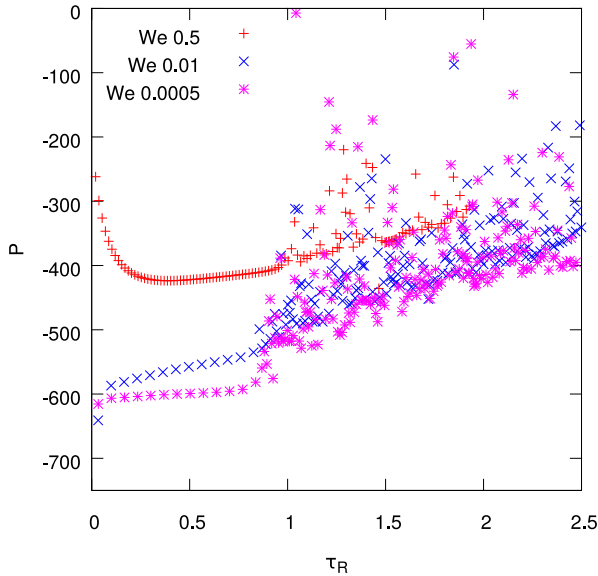


Fig. 14. The average pressure in the domain as a function of time for the three simulations with different We .

of no consequence in the incompressible flow assumption, as we could raise the entire field's pressure by some scalar value without changing the physics. Next, we will study the effect of varying the void fraction growth rate.

4.3. Multiple bubbles with varying We

In this section the results of three test cases with $N_0 = 365$ initial bubbles in an expanding domain will be illustrated. The simulation parameters used for these tests are given in Table 3. By varying the normal outflow velocity U_n , different expansion rates ω are obtained. Three velocities U_n are considered, 5.5×10^{-3} ,

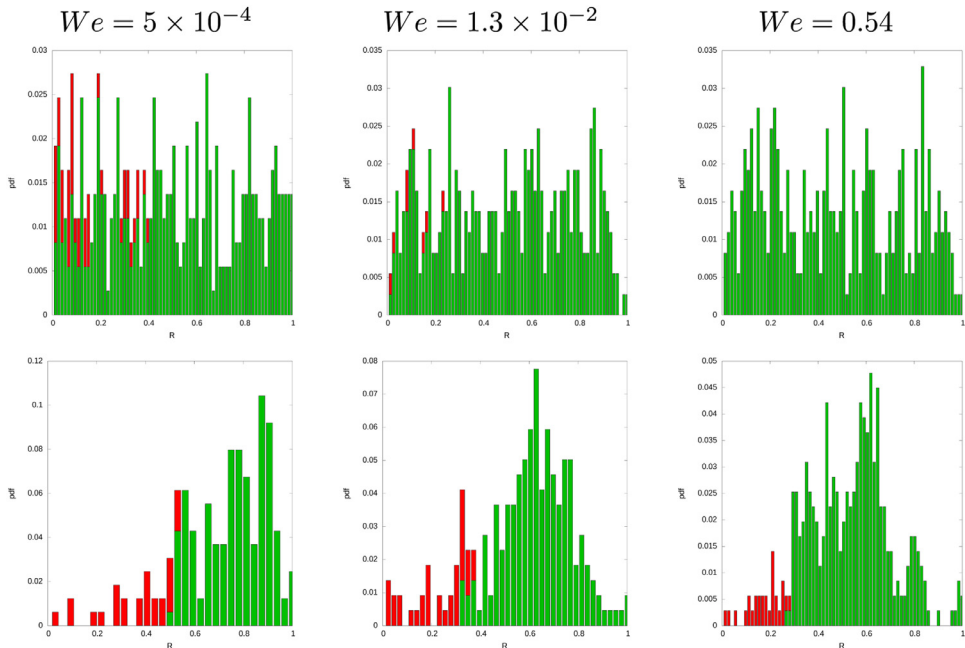


Fig. 15. Distribution of bubble radii, normalized to the maximum radius at that particular time. Bubbles that are growing are shown in green, while bubbles that are shrinking are shown in red. The first row shows the initial distribution and the second one after 3000 time steps. (For interpretation of the references to colour in this figure legend, the reader is referred to the web version of this article.)

2.75×10^{-2} and 1.75×10^{-1} , in turn corresponding to the three Weber numbers, 5×10^{-4} , 1.3×10^{-2} and 0.54 , of Table 3.

The effect of We on the simulation results can be appreciated in Fig. 12, where individual bubble volumes are plotted against the total void fraction instead of time, since with constant outflow rates the void fraction is directly proportional to time. It is observed that the higher the Weber number, the later the bubble collapse occurs and the number of bubble collapses at a given total void fraction decreases with increasing We . This means that the higher the Weber number, the more uniform the growth rate of individual bubbles and consequently fewer bubbles collapse as the total void fraction increases.

Fig. 13 shows screen shots at progressive time steps. A bubble competition is observed: some larger bubbles tend to grow at the demise of smaller ones. The two-dimensional slices on the right show a number of bubbles, with the colour scale indicating the pressure. A pressure gradient is formed in the liquid from the large bubbles towards the smaller ones. The average pressure also increases with time, in a way similar to that observed in the zero We case. An average pressure evolution plot is presented in Fig. 14 for the average pressure in the three cases.

The bubble radius distribution is presented in Fig. 15. Initially all bubbles expand in the high We case.

4.4. Bubble interaction

In this section a proportionality between the time scale of pore competition and the Weber number is formulated. Since the liquid is incompressible, its volume outflow with a constant velocity is balanced by an overall volume expansion of the bubbles in the computational domain, hence we can write

$$\omega L^3 = \sum_{i=1}^N 4\pi R_i^2 \dot{R}_i \quad (33)$$

We now introduce the concept of an average bubble of radius \bar{R} , with an average rate of change of its radius $\dot{\bar{R}}$, which can be considered as representative of the entire population of bubbles. The

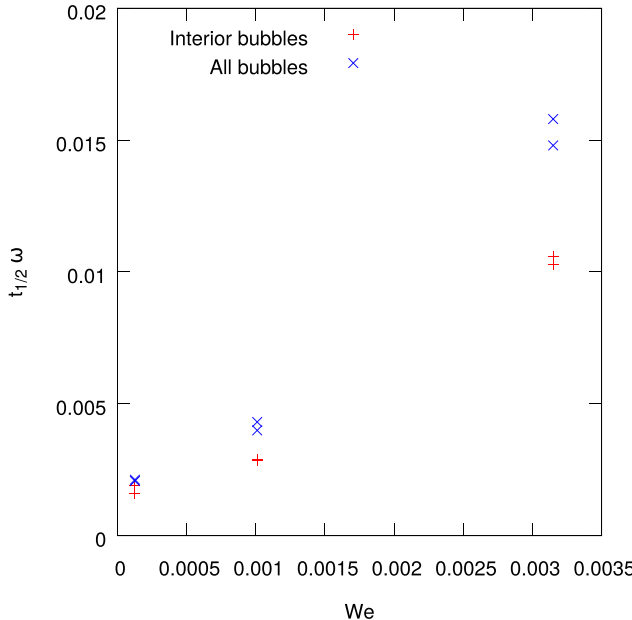


Fig. 16. Comparison of non-dimensional collapse time, $t_{1/2} \omega$, for half of the initial bubbles for the three simulations with different We .

sum of the volume expansion of each bubble can then be written in terms of the growth rate of this average bubble

$$\sum_{i=1}^N 4\pi R_i^2 \dot{R}_i = N 4\pi \bar{R}^2 \dot{\bar{R}}. \quad (34)$$

After substituting (34) in (33), the volume balance equation is integrated in time to give the following evolution expression for the average radius \bar{R}

$$\bar{R}^3(t) = \frac{3\omega L^3 t}{4\pi N} \quad (35)$$

Here it is has been implicitly assumed that $R_{\min} \ll 1$, a condition which is satisfied in our simulations, since bubbles are initialised to be as small as possible.

Let $t_{1/2}$ be the time at which half of the bubbles have collapsed. Using dimensional analysis and assuming that bubble collapse happens on a time scale dictated by the bubble radius length scale, we can write

$$t_{1/2} = \left(\frac{\rho \bar{R}(t_{1/2})^3}{\sigma} \right)^{1/2}. \quad (36)$$

We introduce (35) in this expression and rearrange it to get

$$t_{1/2} \omega = \frac{3\omega^2 \rho \ell_D^3}{4\pi \sigma} = \frac{3}{4\pi} We. \quad (37)$$

This relation was tested for the three simulations with different We and the results are given in Fig. 16. The time $t_{1/2}$ was measured by either considering all the bubbles inside the domain, or by excluding the outermost ones. It is interesting to note that the measured times differ, especially for the higher We case. This indicates a buffering effect exerted by the outermost bubbles leading to different evolution rates for the bubbles towards the interior. The relationship is at least qualitatively linear, but should be confirmed with tests at a wider range of Weber numbers.

5. Conclusion

A numerical tool was presented to deal with the specific problem of bubble interaction in an expanding, incompressible liquid

during the micro-spalling of metals. The code was validated by simulating a single oscillating bubble and comparing it to a higher order numerical solution of the Rayleigh-Plesset equation.

Simulations with hundreds of bubbles were studied for test cases defined by a different Weber number. A bubble competition was observed and the time scale of bubble interaction was found to be dependent on the Weber number.

Acknowledgements

This project was funded by the CEA and simulations were performed on their *Airain* supercomputer at the TGCC facility. We thank them for their kind co-operation.

Visualization and images, like those in Fig. 13 were created using *VisIt* [41]. *VisIt* is supported by the Department of Energy with funding from the Advanced Simulation and Computing Program and the Scientific Discovery through Advanced Computing Program.

The separate numerical solver for the Rayleigh-Plesset equation using a Runge-Kutta time integration scheme was created with the help of Daniel Fuster. Thank you also to Wojciech Aniszewski for valuable feedback during the writing of this paper.

Appendix A. Rayleigh-Plesset equation

A derivation for the governing equation for a bubble with radius R in an inviscid fluid will be detailed here. The flow is assumed to be spherically symmetric and incompressible. First, the velocity \mathbf{u} is written as a function of the general radial coordinate r and the bubble radius R . The continuity equation for incompressible flow is

$$\nabla \cdot \mathbf{u} = 0. \quad (38)$$

For a spherically symmetric flow, the velocity \mathbf{u} is only a function of the radial coordinate r and time t

$$\mathbf{u} = u(r, t) \hat{\mathbf{r}}, \quad (39)$$

where $\hat{\mathbf{r}}$ is the unit radial vector, so the velocity will simply be denoted by the radial component $u(r, t)$.

In general, the velocity at position r can be written as some function of time

$$u = \frac{f(t)}{r^2}. \quad (40)$$

At the interface of the bubble $r = R$, so that $u = f(t)/R^2 = dR/dt = \dot{R}$. Rewriting this equation gives

$$f(t) = \dot{R}R^2 \quad (41)$$

and substituting this back into (40) gives

$$u = \frac{\dot{R}R^2}{r^2} \quad (42)$$

The one-dimensional Euler equation is given by

$$\frac{Du}{Dt} = -\frac{\nabla p}{\rho} \quad (43)$$

Substituting (42) into the above equation gives

$$\frac{\ddot{R}R^2 + 2R\dot{R}^2}{r^2} - \frac{2\dot{R}^2 R^4}{r^5} = -\frac{1}{\rho_l} \frac{dp}{dr}, \quad (44)$$

with ρ_l the liquid density.

This equation can now be integrated from the bubble interface at R , where the pressure is p_R to infinity at pressure p_∞ :

$$\begin{aligned} \ddot{R}R + \frac{3}{2}\dot{R}^2 &= \frac{p_R - p_\infty}{\rho_l} \\ &= \frac{p_c - 2\sigma/R - p_\infty}{\rho_l}, \end{aligned} \quad (45)$$

with σ the surface tension coefficient and the pressure jump from surface tension accounted for.

A1. Pressure at a finite distance

We are interested in knowing the spatial pressure distribution in order to set the pressure on the boundary of a numerical simulation. Starting from Eq. (44), we now integrate in space from the bubble surface at R to any r , with respective pressures p_R and $p(r)$. An expression is then obtained for p as a function of r which can be used to set the pressure at some finite distance

$$p(r, t) = p_R - \rho_l \left(\frac{\dot{R}^2 R^4}{2r^4} - \frac{\ddot{R}R^2 + 2R\dot{R}^2}{r} - \frac{\dot{R}^2}{2} + \ddot{R}R + 2\dot{R}^2 \right), \quad (46)$$

with $p_R = p_c - \frac{2\sigma}{R}$.

References

- [1] Andriot P, Chapron P, Lambert V, Olive F. Influence of melting on shocked free surface behaviour using Doppler laser interferometry and X-ray densitometry. Elsevier Science The Netherlands; 1983. p. 277–80.
- [2] Signor L. Contribution à la caractérisation et à la modélisation du micro-écaillage de l'étain fondu sous choc. Ecole Nationale Supérieure de Mécanique et d'Aérotechnique; 2008.
- [3] Signor L, Dragon A, Roy G, De Rességuier T, Llorca F. Dynamic fragmentation of melted metals upon intense shock wave loading. some modelling issues applied to a tin target. *Arch Mech* 2008;60(4):323–43.
- [4] Signor L, Lescoute E, Loison D, De Rességuier T, Dragon A, Roy G. Experimental study of dynamic fragmentation of shockloaded metals below and above melting. In: ICEM 14 – 14th International Conference on Experimental Mechanics, Poitiers, France, Edited by Fabrice Brémand; EPJ Web of Conferences, 6; 2010. p. 39012.
- [5] De Rességuier T, Lescoute E, Morard G, Guyot F. Dynamic fragmentation as a possible diagnostic for high pressure melting in laser shock-loaded iron. In: Shock Compression of Condensed Matter 2009: Proceedings of the American Physical Society Topical Group on Shock Compression of Condensed Matter AIP Conference Proceedings, 1195; 2009. p. 1007–10.
- [6] De Rességuier T, Loison D, Lescoute E, Signor L, Dragon A. Dynamic fragmentation of laser shock-melted metals: some experimental advances. *J Theor Appl Mech* 2010;48:957–72.
- [7] Fuster D, Pham K, Zaleski S. Stability of bubbly liquids and its connection to the process of cavitation inception. *Phys Fluids* 2014;26(4):042002,1–11.
- [8] Signor L, de Rességuier T, Dragon A, Roy G, Fanget A, Faessel M. Investigation of fragments size resulting from dynamic fragmentation in melted state of laser shock-loaded tin. *Int J Impact Eng* 2010;37(8):887–900.
- [9] Stebnovskii SV. Generalized rheological model of cavitating condensed media. *J Appl Mech Tech Phys* 2001;42(3):482–92.
- [10] Stebnovskii NA. Formation conditions for bubble suspensions upon shock-wave loading of liquids. *J Appl Mech Tech Phys* 2000;41(2):251–60.
- [11] Stebnovskii SV. Generalized rheological model of shear deformation of structured condensed media. *J Appl Mech Tech Phys* 2007;48:694–700.
- [12] Watanabe M, Prosperetti A. Shock waves in dilute bubbly liquids. *J Fluid Mech* 1994;274:349–81.
- [13] Popinet S, Zaleski S. Bubble collapse near a solid boundary: a numerical study of the influence of viscosity. *J Fluid Mech* 2002;464(01):137–63.
- [14] Sussman M. A second order coupled level set and volume-of-fluid method for computing growth and collapse of vapor bubbles. *J Comput Phys* 2003;187:110–36.
- [15] Can E, Prosperetti A. A level set method for vapor bubble dynamics. *J Comput Phys* 2012;231:1533–52.
- [16] Delale CF, Nas S, Tryggvason G. Direct numerical simulations of shock propagation in bubbly liquids. *Phys Fluids* 2005;17:121705,1–4.
- [17] Rossinelli D, Hejazialhosseini B, Hadjidoukas P, Bekas C, Curioni A, Bertsch A, et al. 11 pflop/s simulations of cloud cavitation collapse. In: High Performance Computing, Networking, Storage and Analysis (SC), 2013 International Conference; 2013. p. 1–13.
- [18] Szymczak WG, Rogers JCW, Solomon JM, Bergert AE. A numerical algorithm for hydrodynamic free boundary problems. *J Comput Phys* 1993;106(2):319–36.
- [19] Hirt CW, Nichols BD. Volume of fluid (VOF) method for the dynamics of free boundaries. *J Comput Phys* 1981;39:201–25.
- [20] Harlow FH, Welch JE. Numerical calculation of time-dependent viscous incompressible flow of fluid with free surface. *Phys Fluids* 1965;8:2182–9.
- [21] Chorin AJ. On the convergence of discrete approximations to the Navier-Stokes equations. *Math Comput* 1969;23(106):341–53.
- [22] DeBar R. Fundamentals of the KRAKEN code. Tech. Rep.. Lawrence Livermore Laboratory, UCIR-760; 1974.
- [23] Aulisa E, Manservisi S, Scardovelli R, Zaleski S. Interface reconstruction with least-squares fit and split advection in three-dimensional cartesian geometry. *J Comput Phys* 2007;225(2):2301–19.
- [24] Scardovelli R, Zaleski S. Analytical relations connecting linear interfaces and volume fractions in rectangular grids. *J Comput Phys* 2000;164(1):228–37.
- [25] Li J. Calcul d'interface affine par morceaux. Comptes rendus de l'Académie des sciences Série II, Mécanique, physique, chimie, astronomie 1995;320(8):391–6.
- [26] Weymouth GD, Yue DK-P. Conservative volume-of-fluid method for free-surface simulations on cartesian-grids. *J Comput Phys* 2010;229:2853–65.
- [27] Esmaeeli A, Tryggvason G. Computations of film boiling. part i: numerical method. *Int J Heat Mass Transf* 2004;47(25):5451–61.
- [28] Fedkiw RP, Aslam T, Merriman B, Osher S. A non-oscillatory eulerian approach to interfaces in multimaterial flows (the ghost fluid method). *J Comput Phys* 1999;152(2):457–92.
- [29] Kang M, Fedkiw RP, Liu X-D. A boundary condition capturing method for multiphase incompressible flow. *J Sci Comput* 2000;15(3):323–60.
- [30] Herrmann M. A parallel Eulerian interface tracking/Lagrangian point particle multi-scale coupling procedure. *J Comput Phys* 2010;229(3):745–59.
- [31] Chan RKC, Street RL. A computer study of finite-amplitude water waves. *J Comput Phys* 1970;6(1):68–94.
- [32] Rudman M. Volume-tracking methods for interfacial flow calculations. *Int J Numer Methods Fluids* 1997;24(7):671–91.
- [33] Boria G, Cervone A, Manservisi S, Scardovelli R, Zaleski S. On the properties and limitations of the height function method in two-dimensional cartesian geometry. *J Comput Phys* 2011;230:851–62.
- [34] Popinet S. An accurate adaptive solver for surface-tension-driven interfacial flows. *J Comput Phys* 2009;228(16):5838–66.
- [35] Leonard BP. A stable and accurate convective modelling procedure based on quadratic upstream interpolation. *Comput Methods Appl Mech Eng* 1979;19:59–98.
- [36] Harten A, Osher S, Engquist B, Chakravarthy SR. Some results on uniformly high-order accurate essentially nonoscillatory schemes. *Appl Numer Math* 1986;2:347–77.
- [37] Shu C-W. High order weighted essentially nonoscillatory schemes for convection dominated problems. *SIAM Rev* 2009;51:82–126.
- [38] Plesset MS, Prosperetti A. Bubble dynamics and cavitation. *Annu Rev Fluid Mech* 1977;9(1):145–85.
- [39] Bnà S, Manservisi S, Scardovelli R, Yecko P, Zaleski S. Numerical integration of implicit functions for the initialization of the VOF function. *Comput Fluids* 2015;113:42–52.
- [40] Bnà S, Manservisi S, Scardovelli R, Yecko P, Zaleski S. Vofi – a library to initialize the volume fraction scalar field. *Comput Phys Commun* 2016;200:291–9.
- [41] Childs H, Brugger E, Whitlock B, Meredith J, Ahern S, Pugmire D, et al. Visit: an end-user tool for visualizing and analyzing very large data. In: High Performance Visualization-Enabling Extreme-Scale Scientific Insight; 2012. p. 357–72.